Narrowband Oscillations in the Upper Equatorial Ocean. Part I: Interpretation as Shear Instabilities

J. N. MOUM, J. D. NASH, AND W. D. SMYTH

College of Oceanic and Atmospheric Sciences, Oregon State University, Corvallis, Oregon

(Manuscript received 17 February 2010, in final form 12 November 2010)

ABSTRACT

Extended measurements of temperature fluctuations that include the turbulence wavenumber band have now been made using rapidly sampled fast thermistors at multiple depths above the core of the Equatorial Undercurrent on the Tropical Atmosphere Ocean (TAO) mooring at 0°, 140°W. These measurements include the signature of narrowband oscillations as well as turbulence, from which the temperature variance dissipation rate χ_T and the turbulence energy dissipation rate ϵ_χ are estimated.

The narrowband oscillations are characterized by the following:

- groupiness—packets consist of $O(10)$ oscillations;
- spectral peaks of up to two orders of magnitude above background;
- a clear day–night cycle with more intensive activity at night;
- enhanced mixing rates;
- frequencies of $1–2 \times 10^{-3}$ Hz, close to both the local buoyancy and shear frequencies, $N/2\pi$ and $S/2\pi$, which vary slowly in time;
- high vertical coherence over at least 30-m scales; and
- abrupt vertical phase change ($\pi/2$ over <20 m).

The abrupt vertical phase change is consistent with instabilities formed in stratified shear flows. Linear stability analysis applied to measured velocity and density profiles leads to predicted frequencies that match those of the observed oscillations. This correspondence suggests that the observed oscillation frequencies are set by the phase speed and wavelength of instabilities as opposed to the Doppler shifting of internal gravity waves with intrinsic frequency set by the local stratification N.

1. Introduction

Because of the importance of turbulent heat and momentum transports to the dynamics of the equatorial current system (Crawford and Osborn 1981; McCreary 1981), experiments to examine the nature of mixing in the central equatorial Pacific were conducted in 1984 (Tropic Heat), 1987 (Tropic Heat 2), 1991 [Tropical Instability Wave Experiment (TIWE)], and autumn 2008. From these experiments, we gained detailed glimpses into the complexity of small-scale processes within the equatorial current system. The intense diurnal cycle of mixing extending beneath the mixed layer was first observed in 1984 (Moum and Caldwell 1985; Gregg et al. 1985) and later found (in 1987) to be associated with intermittently occurring bursts of oscillations with frequencies near the local buoyancy frequency (McPhaden and Peters 1992) and horizontal wavelengths of 150–250 m (Moum et al. 1992a). Recently, surprisingly intense subsurface mixing was observed above the core of the Equatorial Undercurrent (EUC) in association with tropical instability waves (Moum et al. 2009); this mixing does not cycle on a daily basis.

There are several ways that narrowband oscillations (frequencies near N, 200-m wavelengths) may be generated; candidates include shear instability in the stratified fluid above the EUC core (Sun et al. 1998; Mack and Hebert 1997; Smyth and Moum 2002), shear instabilities formed in the mixed layer when shear is enhanced by easterly wind intensifications (Skyllingstad and Denbo 1994), convectively driven eddies in the mixed layer (Gregg et al. 1985), and an obstacle effect associated with sheared flow over a perturbed mixed layer base

Corresponding author address: J. N. Moum, College of Oceanic and Atmospheric Sciences, Oregon State University, COAS Admin. Bldg. 104, Corvallis, OR 97331-5503.
E-mail: moum@coas.oregonstate.edu

DOI: 10.1175/2010JPO4450.1

(Wijesekera and Dillon 1991). It is possible that different instability mechanisms occur at different times (or even simultaneously). It is important for us to determine exactly how these instabilities occur to make the link to the next larger temporal and spatial scales, which is the way we will improve mixing parameterizations.

We have recently demonstrated a new means of obtaining moored measurements of mixing (Moum and Nash 2009) that consists of a pair of fast-response thermistors protruding from a pressure case attached to a mooring cable. The instrument, which we call χpod, is vaned to steer the thermistors into the flow, thus permitting measurement of undisturbed turbulence. This has proven successful at current speeds above 0.05 m s^{-1}. The technique is especially useful in the upper equatorial current system, where strong currents prevail.

The purpose of these measurements is to obtain records of mixing that are sufficiently long to evaluate the interplay between mixing, waves, and the larger circulation scales that affect interannual phenomena such as El Niño and La Niña. Long time series are required because attempts to parameterize mixing from the intensive but short equatorial turbulence profiling experiments to date have not been particularly successful (Zaron and Moum 2009). We suggest that this is partly because our limited experiments have not measured the full range of equatorial mixing states.

A complementary set of objectives includes obtaining a useful measure of the turbulent heat flux over long time scales to allow estimates of the vertical divergence and thus heating rates through the water column. In this way, we anticipate determining the role that variations in mixing have on the large-scale equatorial current structure and particularly on the sea surface temperature (SST).

Here we examine an 8-month record from four depths above the core of the EUC with the intention of pointing out the variety of states of mixing and how these are related to narrowband oscillations, which are ubiquitous in these time series. We are hesitant to refer to these a priori as ''internal waves,'' because we wish to distinguish freely propagating internal gravity waves from shear instability waves and hence use the term ''oscillation'' to cover both phenomena.

We begin with a short description of the data (section 2) and the background oceanographic conditions during the deployment (section 3). We then take a closer look at a 52-day portion of the record that most clearly contains the narrowband signal in order to examine the temperature variability and properties of the narrowband oscillations (section 4) and their relationship to turbulence (section 5). A discussion follows in which we argue that these observations are consistent with shear instabilities, which prompts a linear stability analysis (LSA) using observed currents and stratification, resulting in the finding that the observed peak frequencies of narrowband oscillations are determined by the phase speeds and wavelengths of shear instabilities formed above the EUC core (section 6). This is followed by a short discussion (section 7) and a summary and conclusions (section 8). In the companion paper (Smyth et al. 2011, hereafter Part II), the computational method for the LSA is presented, the computed instabilities are described in greater detail, and a theory is advanced to explain the narrowband character of the oscillations.

2. Details of the deployment

Five χpods were deployed on the Tropical Atmosphere Ocean (TAO) mooring at 0°, 140°W on 18 September 2006 at 29-, 39-, 49-, 59-, and 84-m depths (χpod depths are shown on the image plots in Fig. 1). These were recovered on 30 May 2007, and a refurbished set of six χpods were deployed on the replacement mooring. The unit targeted for 84 m was damaged prior to deployment and no data were recorded. All of the other units provided continuous data for the duration of the deployment. The χpods provided temperature at 10-Hz sample rate and its derivative at 120 Hz. Using currents measured nearby and the cable motion as sensed by linear accelerometers on board the χpods, the flow speed past the sensors is determined. The temperature variance dissipation rate χ_T is then computed as described by Moum and Nash (2009). From this, we estimate the turbulence kinetic energy dissipation rate ϵ_χ[1] and the turbulence diffusion coefficient for heat K_T.

The background temperature structure in the upper 100 m at 0°, 140°W during the deployment was derived from temperature measurements on the TAO mooring at 1, 5, 10, 13, 20, 25, 28, 40, 45, 48, 60, 80, and 100 m (Fig. 1b). From these, an estimate of mixed layer depth was made as the depth at which the temperature deviated from its value at 1 m by 0.15 K (daily maxima of mixed layer depths are shown in Fig. 1b). Wind stress (Fig. 1a) was derived from wind speed measurements on the surface float using bulk formulas (Fairall et al. 1996). A nearby subsurface mooring with 150-kHz narrowband acoustic Doppler current profiler (ADCP) at 270-m depth provided a measure of ambient currents in the upper 250 m (zonal u and meridional v currents are shown in Figs. 1c,d, and squared shear computed from these in Fig. 1e), augmented by discrete measurements on the surface mooring

[1] The subscript χ is used to indicate that ϵ is computed from microscale temperature, not shear.

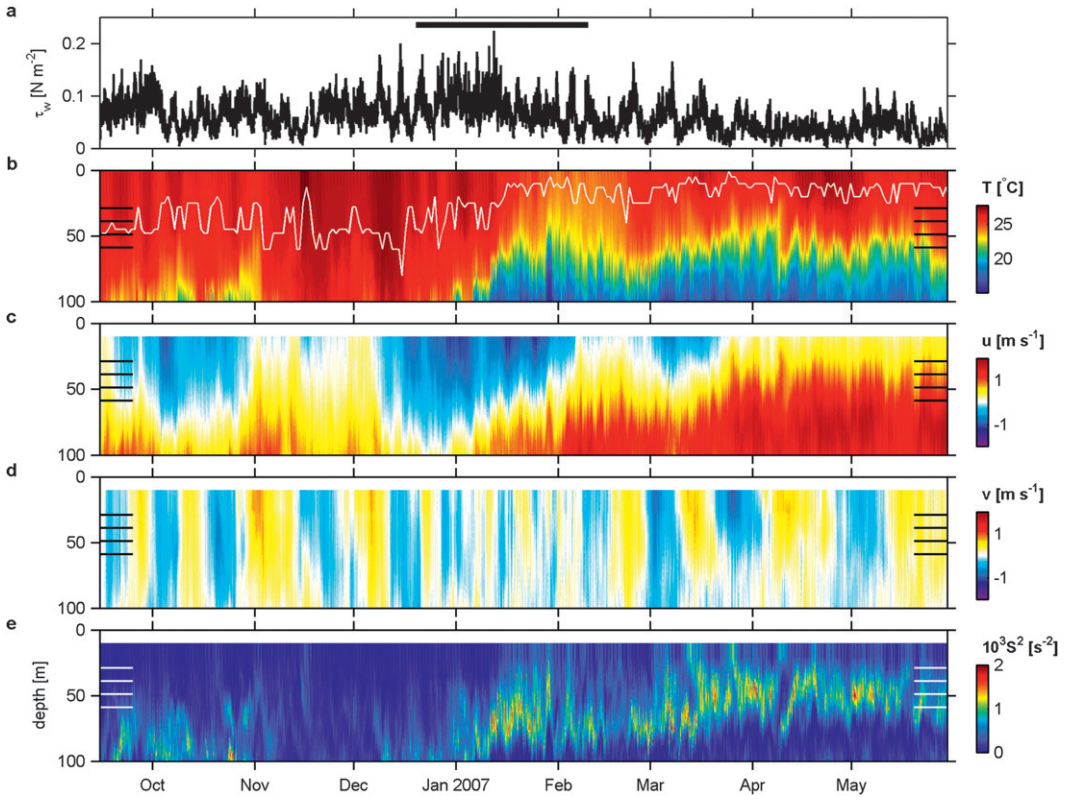

FIG. 1. (a) Wind stress τ_w at 0°, 140°W from mid-September 2006 to end of May 2007. (b) Temperature in upper 100 m (image color); daily maximum mixed layer depth (defined as the depth where temperature deviates from SST by 0.15 K) is the white line. (c) Zonal velocity, (d) meridional velocity, and (e) squared shear. The χpod depths are denoted by the short horizontal lines at both abscissa extrema of (b)–(e). The bar at the top of (a) refers to the time period of further focus in the present analysis.

in the upper 40 m, where sidelobe contamination affects the ADCP measurement. The subsurface mooring is part of the standard TAO project array at this location. Data are provided as 15-min averages at 1-h intervals with 8-m vertical bins.

The local buoyancy frequency N is computed in two ways. A large-scale estimate is derived from temperature and conductivity measurements on the TAO mooring. The spacing of temperature sensors is given in the previous paragraph. Conductivity sensors were spaced at 20-m intervals in the 20–60-m depth range that includes our χpods. These measurements were interpolated to 5-m vertical spacing and density ρ was computed; from this, $N^2 = -g\rho_z/\rho$, where ρ_z is the local vertical density gradient and g is the acceleration due to gravity. For the purpose of this analysis, this estimate of N is used for time-averaged, vertical profiles. An estimate of N that is local in both time and space to our χpods and does not require differencing measurements from independent sensors (an operation that amplifies uncertainties in gradients) is derived directly from χpod measurements of T. Vertical pumping of the TAO mooring by surface gravity waves acting on the surface float causes the χpods to move vertically (nominally, ±1.5 m) about their mean depth on the mooring (Moum and Nash 2009). Here T is fit to z over 2-min intervals from which the local vertical gradient T_z is derived. From this follows $N_T^2 = g\alpha T_z$, where α is the thermal expansion coefficient of seawater. The terms N and N_T are compared in section 4. Because it turns out that the contribution from salinity gradients is small during the periods of greatest interest and because N_T provides a local estimate uncompromised by interpolation, we employ this value in combination with wave displacement in section 4 to estimate wave energy. Here N_T is also used in the χpod estimate of χ_T and ϵ_χ, as prescribed by Moum and Nash (2009). Again, during the periods of interest, χ_T and ϵ_χ are found not to be biased by our choice of N. Uses of N and N_T are clearly distinguished in the figures and text to follow.

3. Background conditions

The variability in Fig. 1 reflects the great range of equatorial motions. Deep mixed layers preceded the

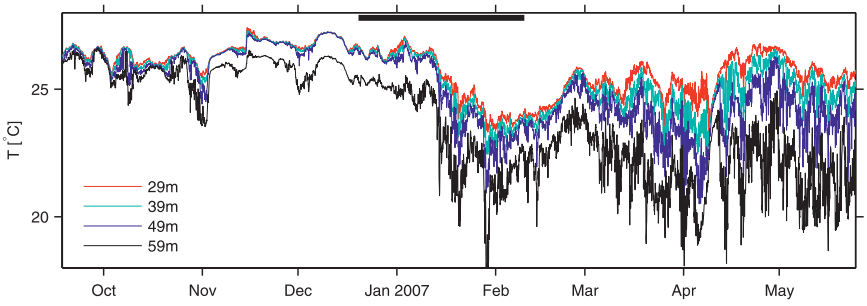

FIG. 2. Temperature records at 29, 39, 49, and 59 m from 18 Sep 2006 to 30 May 2007 as measured by χpods on the 0°, 140°W TAO mooring. The bar at the top refers to the time period of further focus in the present analysis.

surfacing of the EUC in early 2007; shallower mixed layer depths followed. Accompanying the surfacing of the EUC is the shallowing of a deeper sustained shear layer above the EUC core into the depth range of the χpods (denoted in Figs. 1b–e). The temperature record at each of the four χpods is shown in Fig. 2. The χpod temperatures indicate good agreement with nearby (1-m offset) temperature sensors on the TAO mooring, typically within a simple offset of 0.1°C.

4. Signatures of the narrowband wave field

The temperature signals shown in Fig. 2 include a highly energetic narrowband signal of varying intensity. This signal is particularly clear in a 52-day period from late December to early February 2007, as illustrated using variance-preserving spectrograms of T (Fig. 3). For this reason and because the longer record obscures daily variations in images such as Fig. 3, we restrict our

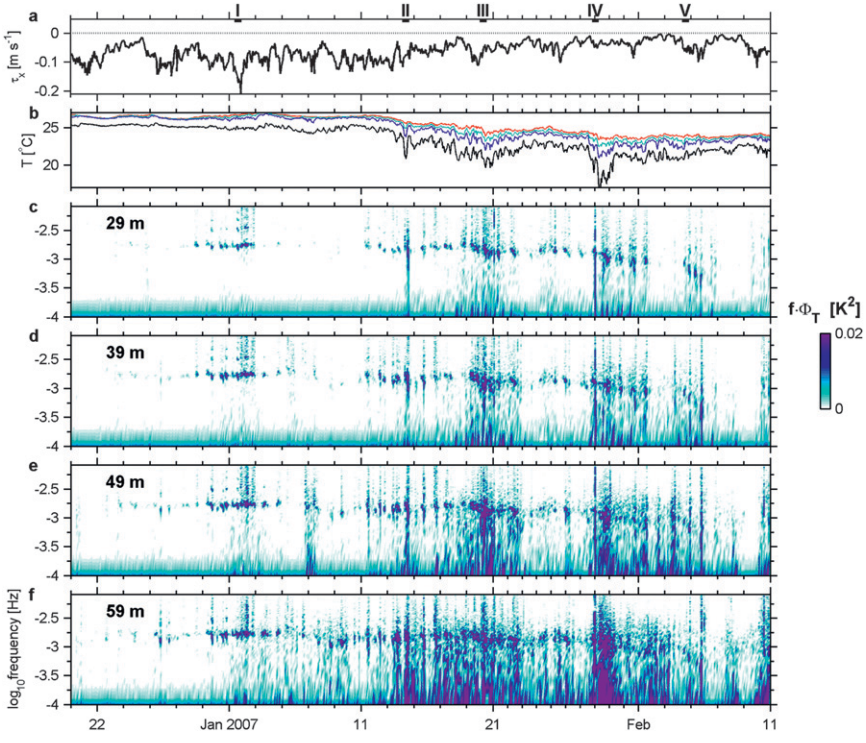

FIG. 3. (a) Wind stress τ, (b) hourly temperature and spectrograms of temperature in variance-preserving form at (c) 29, (d) 39, (e) 49, and (f) 59 m from 20 Dec 2006 to 10 Feb 2007. The bars and roman numerals at the top of (a) represent 12 h examples reproduced in detail in Fig. 8. In these images, the narrowband spectral peaks appear as bright blue streaks in the vicinity of $f = 10^{-3}$ Hz.

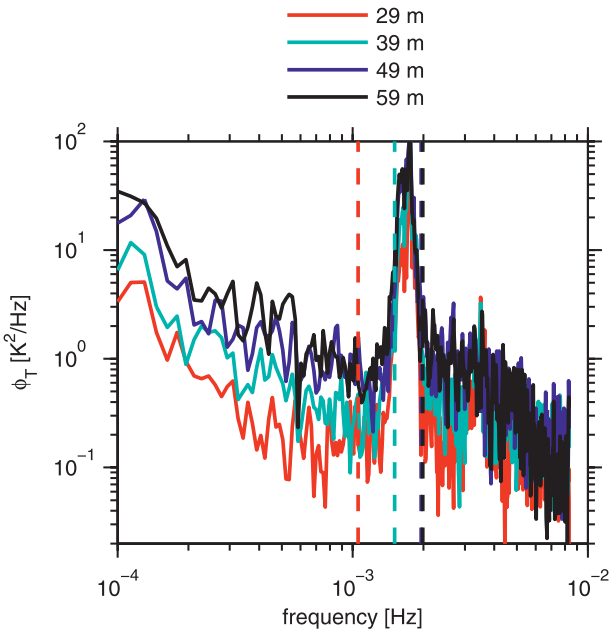

FIG. 4. Temperature spectra (from 1 min data) at 29, 39, 49, and 59 m for the two-day period shown in Fig. 6. Vertical dashed lines represent local buoyancy frequency, $N/2\pi$, at each depth.

attention to this 52-day period for the remainder of this analysis. The narrowband signal is seen as a peak at approximately 0.002 Hz at the beginning of January 2007, slightly greater than $N/2\pi$. The narrowband spectral peak pulses at the diurnal period and decreases in frequency throughout the month of February to approximately 10^{-3} Hz. Averaged spectral amplitudes over a two-day period (1–3 January 2007) are about two orders of magnitude greater at frequencies between 1.5 and 2×10^{-3} Hz than at background frequencies (Fig. 4). Note that the frequencies of elevated variance are the same for each depth and are not specifically linked to the local buoyancy frequency, which varies considerably in depth (denoted by the vertical dashed lines in Fig. 4).

The frequency at the amplitude maxima in Fig. 3 is identified by finding the peak in each spectrum and requiring it to have a minimum amplitude of 2.3×10^{-3} K^2; we refer to the frequency at this peak as $f_{\rm NB}$. The result for the χpod at 29 m is shown in Fig. 5a. The short-term variability in $f_{\rm NB}$ is significantly smaller than that in $N_T/2\pi$, and the two frequencies are practically uncorrelated (actually weakly correlated in a negative sense, $r = -0.25$).

A comparison between N and N_T is also seen in Fig. 5a. Salinity gradients apparently occur with either sign (interpolated to 29 m) in this record, destabilizing early in the record when stratification is weak and stabilizing at the end of the record. However, during the periods of interest for this study (when $f_{\rm NB}$ is well defined), the effect of salinity gradient on N^2 is reasonably small. We believe the estimate of N^2 from the coarsely spaced and slowly sampled moored sensors is not particularly relevant to local turbulence dynamics, making N_T^2 the relevant stratification for use in the computation of χ_T.

The distinctive peak in temperature spectra suggests that we can fairly reliably extract the narrowband signal by filtering. We define the perturbation temperature signal T' by high-pass filtering the temperature record at 3×10^{-4} Hz. A relative measure of the narrowband displacement is then

$$\zeta = \frac{T'}{T_z}, \tag{1}$$

from which we estimate $N_T^2\zeta^2$ as twice the available potential energy associated with the narrowband oscillations, following Moum et al. (1992a).

A two-day example that shows the variability of the narrowband signal and its relationship to the turbulence is represented in Fig. 6. Unfortunately, the solar radiation signal on the TAO mooring was incomplete for this deployment. To indicate the time of the solar day, an estimate of clear sky, shortwave radiation is shown in Fig. 6a, as determined from a simple model.[2] The duration of narrowband bursts is several hours, most intensely at night. These are typically accompanied by high ϵ_χ. Generally, ϵ_χ is lower when narrowband oscillations are absent. In the first energetic wave group (just past midday on 1 January), the oscillations appear at all depths at close to the same time. However, high ϵ_χ is observed first at the upper χpod and thence progressively later with depth. The other oscillation groups seem to show that both oscillations and turbulence appear at the upper χpod first, following which they appear progressively later with increasing depth.

During the period of the measurements shown in Fig. 6, the core of the EUC was about 125 m deep (Fig. 7a). The four χpods were above the EUC core, in the westward-flowing South Equatorial Current (SEC). The spectral peak at $f_{\rm NB} \simeq 0.0017$ Hz (Fig. 7d) is similar to the local value of $N/2\pi$ (6 cph) at 40–70 m (Fig. 7b), but $f_{\rm NB} > N/2\pi$ at 29 m. Oscillations are vertically coherent at all measurement depths (Fig. 7e), with a strong vertical phase dependence (Fig. 7f). The phase lag at 39 m is approximately $\pi/4$ relative to 29 m, and $\pi/2$ at 49 and 59 m (also relative to 29 m), suggesting that the $\pi/2$ phase shift occurs over a distance of $\Delta_z < 20$ m. These results are similar to

[2] $J_q^{\rm SW} = I_0 \sin\omega_0(t - t_0)$, when $\sin\omega_0(t - t_0) > 0$, where $I_0 = 1100$ W m^{-2}, $\omega_0 = 2\pi$ radians day^{-1}, and $t_0 = 140/360 + 1/4$ days; otherwise, $J_q^{\rm SW} = 0$.

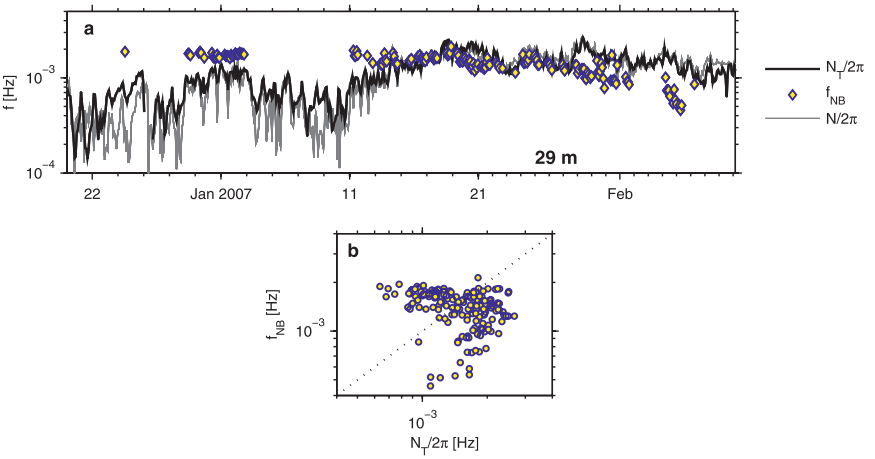

FIG. 5. (a) Time series of $N_T/2\pi$ (black line), f_{NB} (symbols), and $N/2\pi$ (gray line) at 29 m. Here f_{NB} corresponds to the spectral peaks in Fig. 3c. (b) $N_T/2\pi$ vs f_{NB}.

those derived from towed thermistor chain measurements nearby and along the equator in 1987 (Moum et al. 1992a).

The detailed structure of the narrowband oscillations is diverse. Five 12-h examples from the period shown in Fig. 3 are reproduced in Fig. 8 (each example is denoted by a Roman numeral at left in Fig. 8, which is echoed in Fig. 3). Over this time period, the mixed layer shallowed from about 50 to 15 m and the zero-crossing point of the zonal velocity (which separates the EUC from the SEC) shallowed from about 70 to 35 m (Fig. 1). The shallowing of the zero-crossing point of the zonal velocity can be seen in Fig. 8a.

These examples were chosen because each is distinguished by a narrowband spectrum but with unique characteristics that we note in turn.

- Case I: The χpods were all located in the westward-flowing SEC. At 39–59 m, $f_{NB} \approx N/2\pi$; at 29 m, $f_{NB} > N/2\pi$. For reference, the spectrum at 59 m (Fig. 8, case I, panel e) is reproduced in gray in Fig. 8, cases II–V,

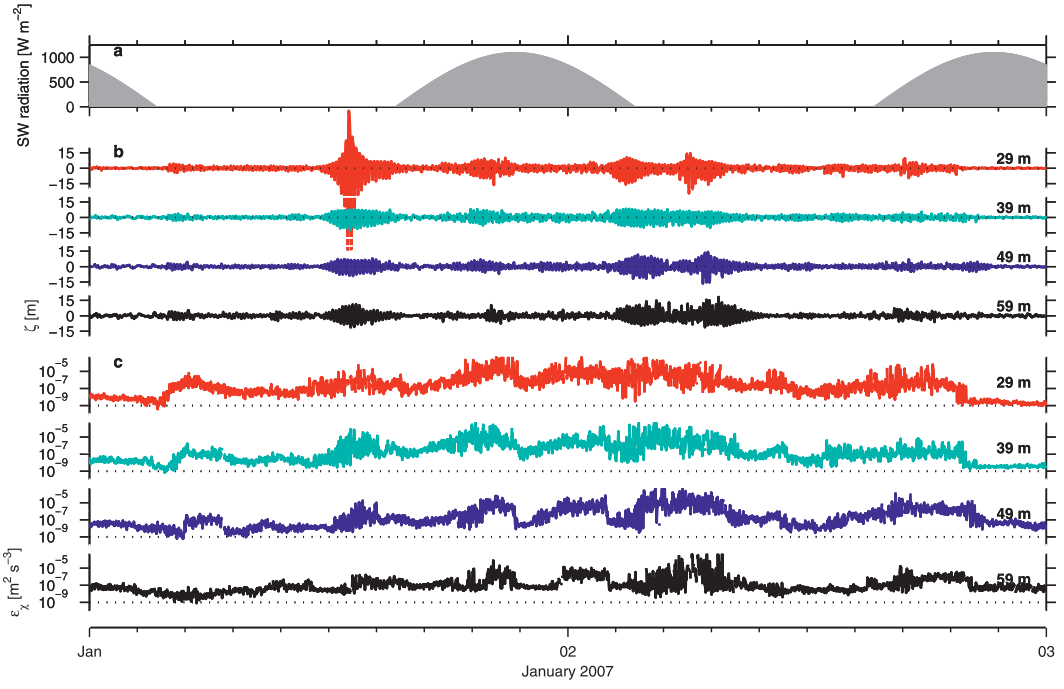

FIG. 6. (a) Incoming shortwave radiation as determined from a clear-sky solar radiation model, (b) ζ (1-min means), and (c) ϵ_χ (1-min averages of 1-s spectral estimates) computed from the four χpods for the first two days of January 2007. In (c), the dotted baselines represent $\epsilon_\chi = 10^{-9}$ m^2 s^{-3}. In this and all plots, times are in UTC.

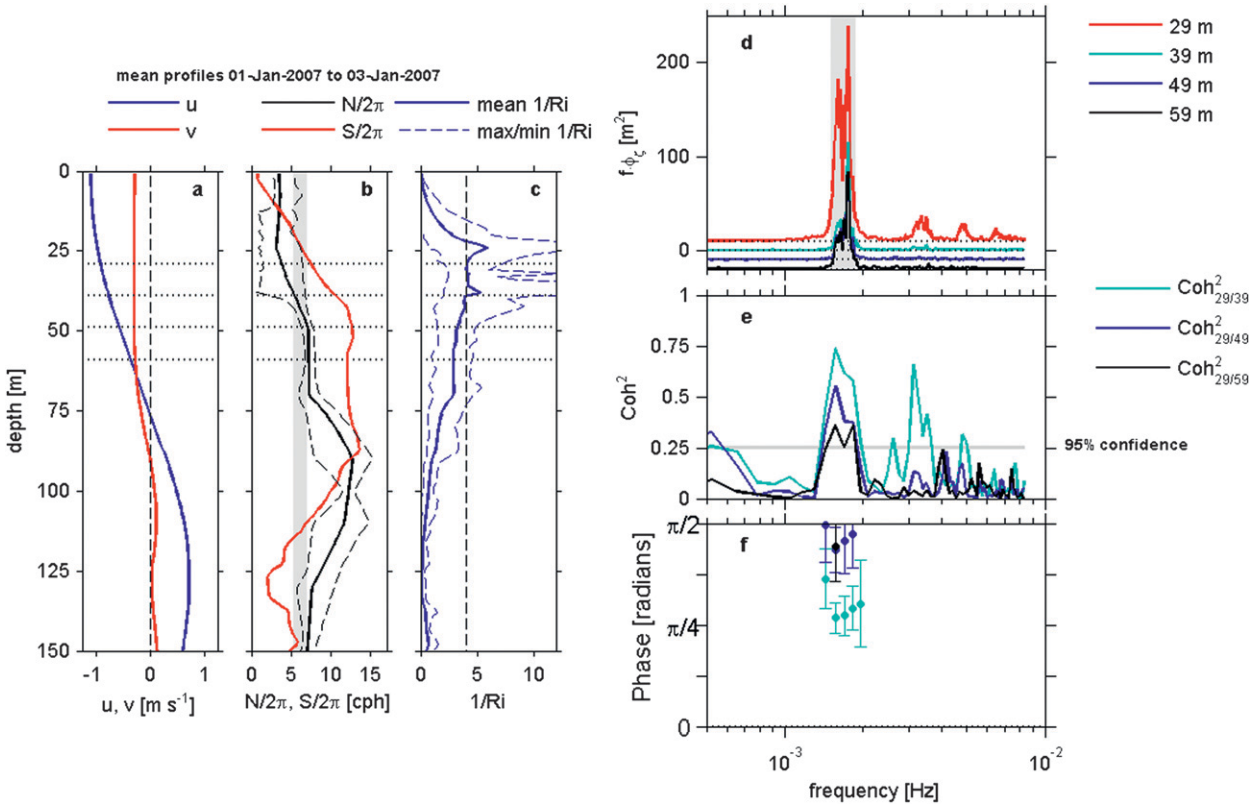

FIG. 7. Averaged profiles for the period shown in Fig. 6. (a) Zonal (u; blue) and meridional (v; red) velocities; (b) buoyancy period (N; black) and shear magnitude (red); and (c) 1/Ri, where the vertical dashed line corresponds to Ri = 1/4, the critical value for shear instability. Spectral characteristics of the wave field are shown: (d) variance-preserving displacement spectra, where the spectral peak is highlighted in gray, which is echoed in (b); (e) squared coherence between displacements at successive depths (95% confidence shown as dotted line); and (f) phase difference relative to 29 m (shown only where coherence is significant and $f \cong f_{NB}$). The 95% confidence limits are indicated. The sign of the phase is such that $0 <$ phase $< \pi$ when the signal at 29-m leads.

panel e. The narrowband signal is most intense in the first half of the record, with oscillations gradually growing in amplitude over the first 12 cycles and then gradually decreasing in amplitude over the final 12 cycles. This is accompanied by a gradual increase and decrease in ϵ_χ.

- Case II: The zero-crossing point of the zonal velocity has shallowed to the depth of the third χpod so that the upper two χpods are in westward-flowing water and the lowest in eastward-flowing water. At all χpod depths, $f_{NB} < N/2\pi$. The dominant signal near the middle of the record consists of oscillations growing in amplitude over approximately 12 cycles, after which they vanish. This abrupt ending is accompanied by an equally abrupt and large increase in ϵ at the depths of the lowest three χpods.
- Case III: Here, f_{NB} is close to that in cases I and II. As in case II, there is significantly greater broadband energy at $f < f_{NB}$ (Fig. 8e, case III) than there is in case I.
- Case IV: This particularly strong event with $f_{NB} > N/2\pi$, at 29 and 39 m, has the signature of the time inverse of case II. That is, initially large amplitude oscillations decrease in amplitude over about 12 cycles. High ϵ_χ accompanies the leading, largest oscillations.
- Case V: In this example of low-frequency oscillations, $f_{NB} < N/2\pi$ at all depths.

5. Relationship to mixing

Two trends are apparent in the 52-day record (20 December 2006–10 February 2007) during which narrowband waves were consistently observed (Fig. 9a). First, there is a clear diurnal cycle in both ϵ_χ and $N_T^2\zeta^2$ (Figs. 9b,c). There is also a modulation of both ϵ_χ and $N_T^2\zeta^2$ on the time scales of the narrowband waves seen in (Fig. 9a). The day–night differences in $N_T^2\zeta^2$ can be seen in histograms of 1-h values sorted into daytime and nighttime periods (Fig. 10). These differences are clear at 29–39 m and marginal deeper.

Because of covariation on both diurnal and longer time scales, $N_T^2\zeta^2$ is highly correlated to ϵ_χ ($r = 0.64$, 95% confidence limits [0.60, 0.69]; Fig. 11). For comparison,

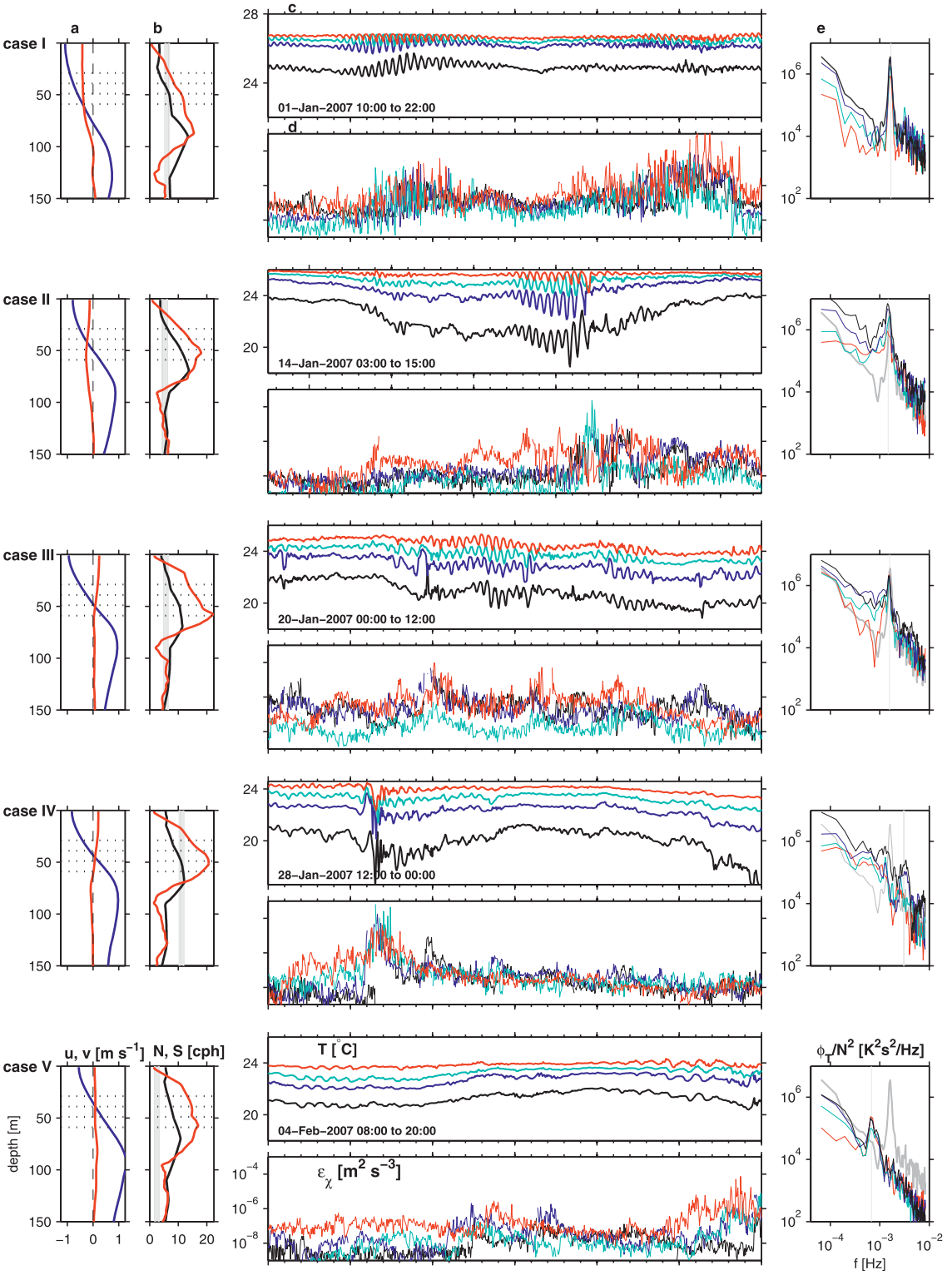

FIG. 8. (a) Averaged zonal (u; blue) and meridional (v; red) velocity profiles. (b) Averaged buoyancy frequency ($N/2\pi$; black) and shear ($S/2\pi$; red) profiles. Averages were computed over (c) the 12-h time periods, which shows temperature at 29- (red), 39- (cyan), 49- (blue), and 59-m (black) depths from the χpods, following the color convention introduced in Fig. 2. (d) ϵ_χ. (e) Temperature spectra normalized by the mean value of N at that depth. The gray spectral line reproduced in all of the plots is the 59-m spectrum from the first (upper) time period. The gray vertical bars in (e) represent the peaks in the spectra and are reproduced in (b).

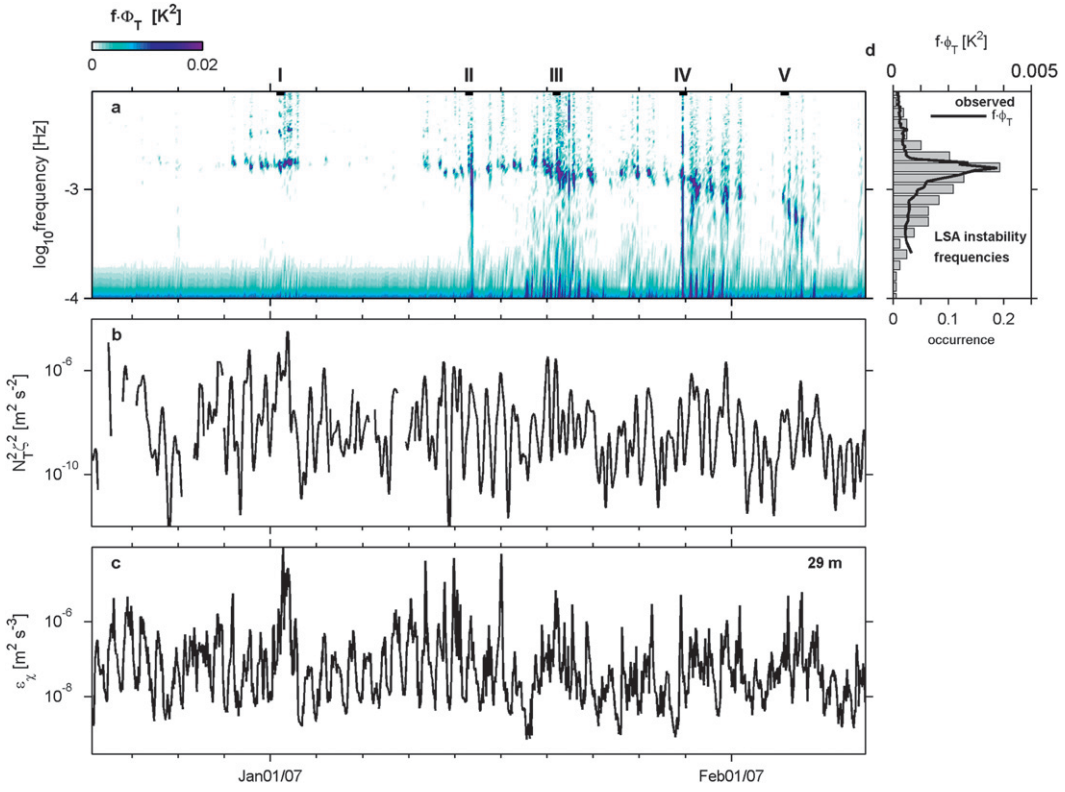

FIG. 9. (a) Temperature spectrogram (variance preserving), (b) $N_T^2\zeta^2$, and (c) ϵ_χ at 29 m for the period 20 Dec 2006–10 Feb 2007. The time periods depicted in Fig. 8 are noted at the top of (a). (d) The histogram corresponds to frequencies estimated from 155 unstable modes as determined from LSA applied to observed profiles of currents and stratification as discussed in section 6a. The solid line in (d) is the temperature spectrum (variance-preserving form) for the full period shown in (a).

the data points plotted in Fig. 9 of Moum et al. (1992a) are also shown ($r = 0.83$). The current χpod estimates overlap the parameter space of the 1987 measurements and extend it.

Lines of unity slope in Fig. 11 represent constant time scales related to the decay of energy $N_T^2\zeta^2$ by turbulence dissipation, $\tau_d \simeq N_T^2\zeta^2/\epsilon$. These suggest that the narrowband oscillations decay rapidly, on a time scale of O(1 h) or a few oscillation periods. This would seem to be consistent with the relatively few oscillations that compose a group as well as the patchiness of the narrowband signal.

6. Mechanistic interpretation

The narrowband signal that we have described from these measurements has several distinctive characteristics. The dominant frequency, $f_{\rm NB} \approx 1\text{–}2 \times 10^{-3}$ Hz, varies remarkably slowly in time (Fig. 3) and is similar in magnitude to both $N/2\pi$ and $S/2\pi$. At times, $f_{\rm NB} > N/2\pi$, although it is not generally observed to be greater than the maximum value of N above the EUC core (Fig. 8).

The oscillations typically appear in groups of about 10 before disappearing from the time series (Fig. 8). The groups are associated with elevated mixing (Fig. 11). Packets appear as both symmetric groups with largest amplitudes and most-elevated mixing in the middle of the group (Fig. 8, case I) and as highly asymmetric groups, with largest amplitudes and most-elevated mixing at either trailing or leading edge (Fig. 8, cases II and IV). If we interpret the oscillations as propagating wave packets, it is impossible to distinguish trailing from leading edge in the time series data.

Signals are vertically coherent over the full depth range of the measurements (29–59 m) and exhibit a change in phase of $\pi/2$ over a vertical span $\leq$20 m. Both of these characteristics were also observed in the towed thermistor chain measurements of Moum et al. (1992a); only the high coherence was detected in the moored observations of McPhaden and Peters (1992). Because of a lack of confidence in relative timing between sensors, McPhaden and Peters (1992) were unable to determine whether vertical differences in phase at the frequencies of the narrowband signal differed from 0.

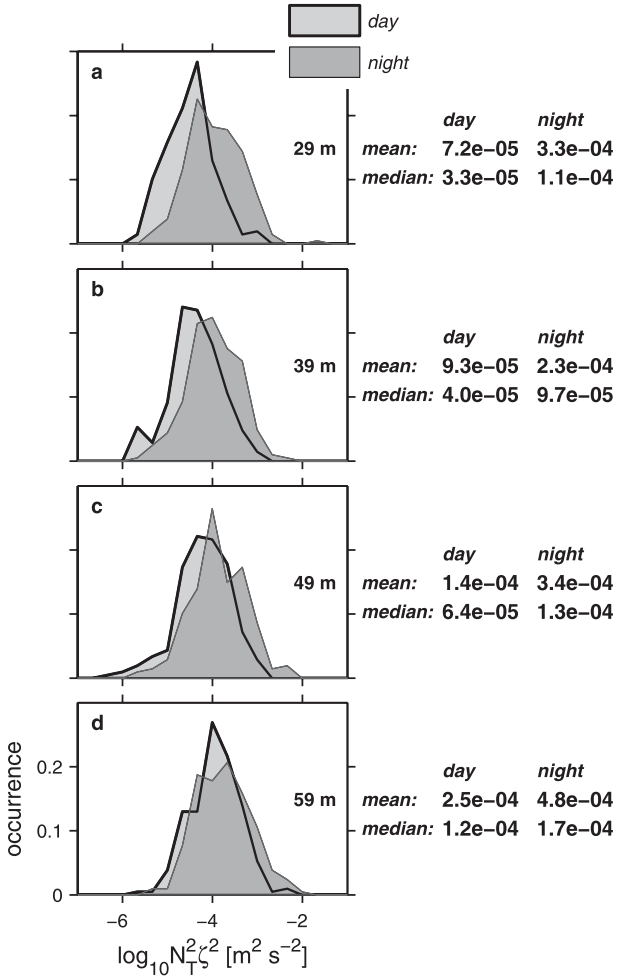

FIG. 10. Histograms of $N_T^2\zeta^2$ at (a) 29-, (b) 39-, (c) 49-, and (d) 59-m depths. These were sorted into daytime (1800–0200 UTC) and nighttime periods (0600–1400 UTC), which are represented by light and dark gray shading, respectively.

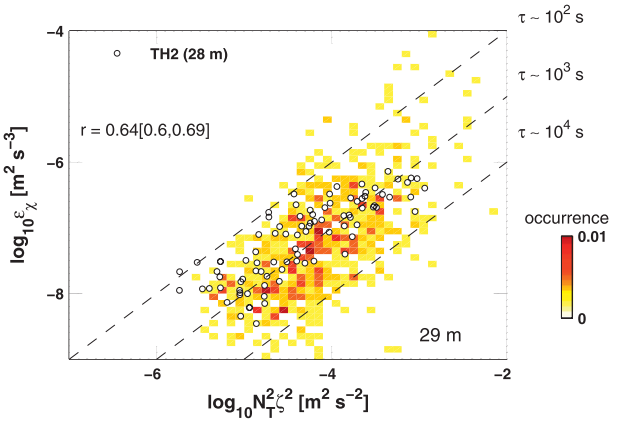

FIG. 11. Comparison of $N_T^2\zeta^2$ and ϵ_χ at 29 m based on 1-h averages over the 52-day period shown in Fig. 9. Yellow/red points plotted represent the two-dimensional histogram; redder points occur more frequently. The black dots represent estimates from measurements in 1987 of ϵ using the turbulence profiler, Chameleon, and a thermistor chain towed behind the ship (Moum et al. 1992a). The correlation for the χpod data is noted at the top left, with 95% confidence limits. The correlation for the 1987 data is 0.83.

In an introduction to the original set of papers describing the narrowband phenomenon beneath the equatorial mixed layer, Moum et al. (1992b) made two significant points. They acknowledged the difficulty in making the distinction between freely propagating internal gravity waves and forced shear instabilities from the observations. They also recognized the importance of doing so, primarily because of the potential for vertical redistribution of momentum by vertically propagating internal waves that would not exist in the case of short-lived shear instabilities.

A number of hypotheses have been proposed to explain this narrowband signal beneath the equatorial mixed layer in the form of internal waves. Wijesekera and Dillon (1991) suggested that the interaction of turbulent overturns in the nighttime mixed layer with the mixed layer base in the highly sheared equatorial current system might produce an internal wave field. From two-dimensional simulations, Skyllingstad and Denbo (1994) showed generation of internal waves in the equatorial surface layer during periods of easterly wind intensifications by shear instabilities generated there. For the data presented here, the shear is generated by easterly winds. In fact, our data show instances of enhancement of narrowband wave activity when easterly winds increase (cf. Figs. 3a,c). However, there are enough counterexamples to indicate that, if easterly wind intensification is a factor, it does not work in isolation. More recently, Pham and Sarkar (2010) have used three-dimensional simulations to show the generation and growth of internal waves by energetic vortex tubes ejected from Kelvin–Helmholtz instabilities into the sheared fluid above the core of the EUC.

At the same time, arguments have been made that the narrowband signal is directly related to shear instabilities. LSA using observed profiles of currents and density (Sun et al. 1998) has shown the generation of shear instabilities with wavelengths close to those observed by Moum et al. (1992a). Most relevant may be the observation of the $\sim\pi/2$ change in phase across the waves, which echoes the results of Moum et al. (1992a) and is expected for growing Kelvin–Helmholtz instabilities (Smyth and Peltier 1989; Baines and Mitsudera 1994). We proceed with this argument by applying LSA to the present data and comparing LSA results with the properties of these observations.

a. Comparison with textbook shear instability

Three rules of thumb arise from studies of the idealized shear instability case of the Kelvin–Helmholtz form growing on a shear layer (e.g., Hazel 1972; Turner 1973):

1) the wavelength is about 7 times the thickness of the shear layer;
2) the phase difference across the shear layer is near $\pi/2$; and
3) the phase speed equals the speed of the background flow where the shear is a maximum and the phase shift is most rapid.

The observed $\pi/2$ phase shift (Fig. 7f) is consistent with property 2 above. The thickness of the layer over which this phase shift occurs provides an estimate for the thickness of the shear layer that generated the instability. In this example, the thickness is $\leq$20 m. For the purpose of rough scaling, we use 20 m. If property 1 above is valid, the resulting wavelength would be 7 times this, or $\lambda \cong 140$ m. This is within the range of wavelengths observed by Moum et al. (1992a), although slightly smaller than the 150–250-m wavelengths that dominated the spectrum.

The phase velocity is likely to be negative because the $\pi/2$ phase change of the disturbance occurs over the depth range of the χpods, which is within the westward-flowing SEC (Figs. 7a,b). To estimate this phase velocity, we use the observed frequency $f_{\mathrm{NB}} = 1.7 \times 10^{-3}$ Hz (Fig. 7d). As defined above, f_{NB} is an absolute value; the actual frequency is negative. We therefore compute the phase velocity as $c = -\lambda f_{\mathrm{NB}} = -0.24$ m s^{-1}. This is within the range of the background velocity (Fig. 7a) in agreement with the semicircle theorem (Howard 1961). It is, however, significantly slower than the background current in the depth range of the χpods where the phase change is observed, contrary to property 3 above. This discrepancy is addressed in section 6b.

In summary, the observed oscillations are consistent with at least some of the well-known properties of Kelvin–Helmholtz instability on a shear layer.

b. LSA of observed mean states

To expand on the results of section 6a, we have carried out stability analyses of hourly averaged profiles of velocity and stratification. The linear stability problem for a viscous, diffusive, stratified, parallel shear flow was solved in matrix form, as described in Part II.

Vertical profiles of current shear and stratification N^2 were computed from the relatively coarsely resolved measurements available from the TAO mooring (Fig. 1). Underresolution of both shear and stratification means that Ri is likely overestimated, as high-resolution measurements show small Ri on vertical scales smaller than the 5-m vertical samples and time scales shorter than the 1-h samples available (Moum et al. 2009). We assume that the hourly averaged profiles represent a stationary, parallel flow perturbed by infinitesimal disturbances, whereas in fact the flow is continuously subjected to large-amplitude perturbations. Despite these caveats, the normal mode spectrum yields a testable prediction of the fastest-growing disturbance.

The LSA yields growth rates and phase speeds as functions of wavenumber. The mode corresponding to the wavenumber where the growth rate is a maximum is the one most likely to reach observable amplitude. The predicted frequency is $f = c/\lambda$, where c and λ are the phase velocity and wavelength of the fastest-growing mode.

This analysis was repeated for all hourly averaged profiles during the time period shown in Figs. 3 and 9, and modes were selected according to criteria given in Part II. The sum of these analyses delivered an ensemble of 155 instability events. It was usually not possible to correlate a specific instability with an observed increase in narrowband signal. This is not surprising for several reasons. First of all, as mentioned earlier, the input data are low resolution. Second, the velocity and density measurements are not collocated. The temperature and conductivity measurements used to compute the stratification were obtained from the TAO surface mooring, which was deployed typically at least 1 km from the subsurface mooring that houses the acoustic Doppler current profiler from which velocity profiles were obtained. Lateral inhomogeneities in currents and stratification between these two locations will contribute to both false positive and false negative indications of instabilities. Third, any observed instability must have had sufficient time to grow to observable amplitude. During this time, it will have propagated at speed c, which is typically $\neq 0$, meaning that the instability was formed elsewhere. Again, lateral inhomogeneities in currents and stratification will contribute to lack of agreement between observed and predicted instabilities. In view of these unavoidable limitations, we focus not on individual events but rather on the statistical properties of the ensemble.

Properties of the 155 unstable modes are discussed in detail in Part II and briefly reviewed here. Growth rates range from 1 to 11 e-foldings per hour (for comparison, a close look at Fig. 6b suggests that the growth rate of the first large packet at midday on 1 January 2007 was approximately 2 e-foldings per hour). As expected from the dominance of zonal shear, unstable modes were generally zonally propagating, with phase velocities ranging from -1 m s^{-1} in the SEC to $+1$ m s^{-1} in the EUC. Negative values were considerably more common, but values close to the peak SEC velocity were rare because modes with critical levels above 37.5-m depth (where the quality

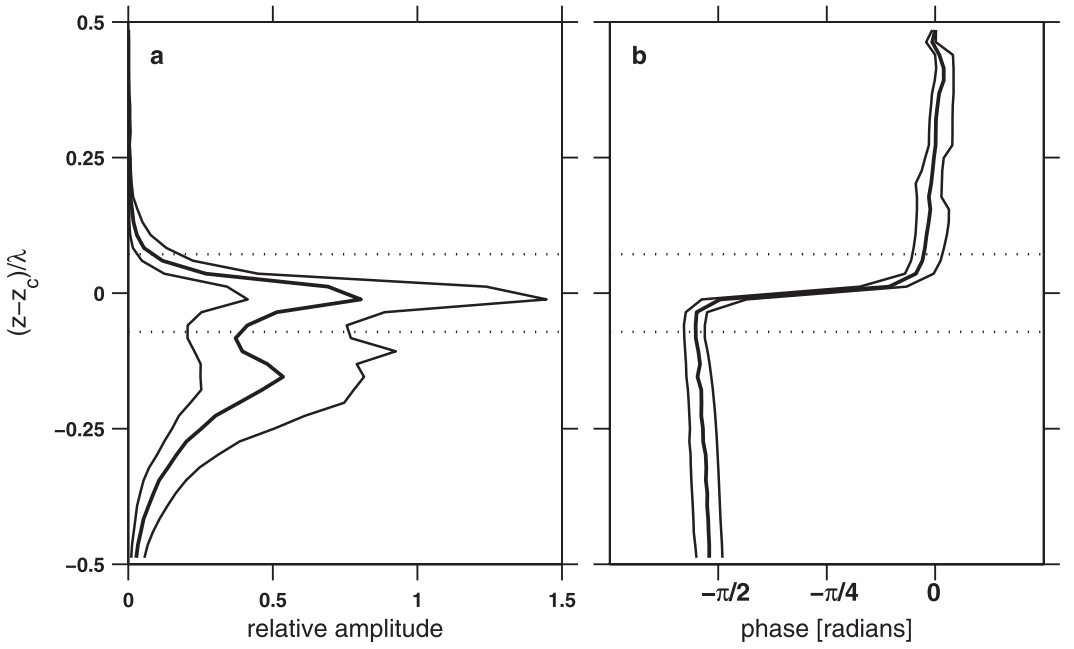

FIG. 12. (a) Amplitude and (b) phase of the vertical displacement eigenfunction corresponding to the 69 fastest-growing modes with frequencies near to the peak frequency in Fig. 9d, as determined from a LSA using observed currents and stratification from TAO mooring data at 0°, 140°W. Amplitude is nondimensional and is defined up to an arbitrary scaling factor. The vertical axis is depth referenced to the critical layer at which the fastest-growing mode was found and nondimensionalized by its wavelength. Horizontal dashed lines identify a layer of thickness $\lambda/7$ about z_c. Thick lines are mean values, and thin lines encompass 50% of the eigenfunctions.

of the TAO velocity measurements was diminished) were rejected. Critical level depths extended nearly to the depth of the EUC core. Although unstable modes could in theory have wavelengths up to 7 times the depth of the EUC core, or 700 m, computed modes all had $\lambda \leq$ 340 m. The computed range of wavelengths is consistent with existing observations (Moum et al. 1992a; Lien et al. 1996).

For the purpose of direct comparison of the properties of observed and predicted instabilities, we compare

- f_{NB} with the apparent frequency $f = c/\lambda$ due to the propagation of computed instabilities past our observation point;
- the vertical phase dependence of the computed instabilities with those observed; and
- predicted wavelengths to estimated shear layer thicknesses, to assess consistency with our first rule of thumb.

1) FREQUENCIES OF SHEAR INSTABILITIES

The ensemble of frequencies determined for the 155 instabilities over the 52-day record shown in Fig. 9a is represented by the histogram in Fig. 9d. Despite the fact that the instabilities arise from a range of critical depths z_c above the core of the EUC, encompassing a range of both c and λ (Part II), the peak frequency of the distribution is very close to that defined by the spectral peak at frequency $f_{\mathrm{NB}} = 1.7 \times 10^{-3}$ Hz (Fig. 9d). Peak frequencies of the observations and computed unstable modes are both close in magnitude to $N/2\pi$ (Fig. 5a) although f_{NB} is not temporally correlated with N (Fig. 5b).

2) VERTICAL PHASE DEPENDENCE

To illustrate the general vertical structure of the instabilities, we computed composite amplitude and phase profiles as follows: We compiled vertical displacement eigenfunctions for 69 unstable modes selected by the requirement that $10^{-3} < |f| < 10^{-2.7}$ Hz, representing the frequency range of the narrowband instabilities (indicated by the mode of the histogram in Fig. 9d). Each vertical displacement eigenfunction was normalized by its value at the critical level. The eigenfunctions were then converted to polar form, and the amplitude and the tangent of the phase were sorted into bins according to the scaled vertical coordinate $(z - z_c)/\lambda$. The median and quartiles were computed for each bin.

Results are shown in Fig. 12. The amplitude peak clearly coincides with z_c in Fig. 12a and the phase changes by close to $\pi/2$ radians across the shear layer, in accord with our second rule of thumb and the observed vertical phase shift (Fig. 7f). Closer inspection of Fig. 12b reveals that the phase shift actually occurs not over the whole

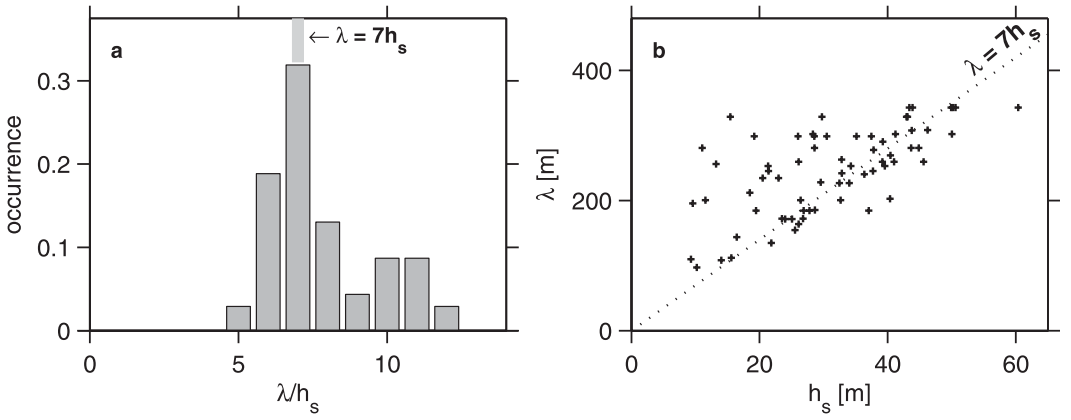

FIG. 13. (a) Histogram of wavelengths nondimensionalized by the thickness of the shear layer h_s in which they were found. Only the 69 modes with absolute frequencies between 10^{-3} and $10^{-2.7}$ Hz were included. (b) Scatterplot of λ vs h_s.

shear layer but over approximately the inner half of that layer. We will show that this property resolves the phase speed discrepancy noted in section 6a.

3) RELATIONSHIP BETWEEN WAVELENGTHS AND SHEAR LAYER THICKNESSES

The shear layer thickness h_s was determined for each mode by fitting the shear magnitude to a function S_0 $\mathrm{sech}^2[(z - z_c)/h_s]$, where S_0 is the shear at the critical level. Figure 13 shows statistics of the shear layer thickness and the wavelength for modes with frequencies in the range $10^{-3} < |f| < 10^{-2.7}$. The median shear layer thickness is 30 m. Combined with our previous observation that the phase shift occurs over half the shear layer, the phase shift should typically occur over 15 m in accordance with the example shown in Fig. 7.

The median wavelength for this subsample of the unstable modes is 245 m, consistent with the observations of Moum et al. (1992a). If we now recompute the phase velocity of the mode shown in Fig. 7 using this wavelength, we find $c = -0.42$ m s^{-1}. This is within the range of background flow speeds observed in the depth range of the χpods. This improved agreement with linear theory is thanks mainly to the refinement of our previous assumption that the phase shift occupies the entire shear layer.

The canonical model for shear layer instability is the Kelvin–Helmholtz form, derived from hyperbolic-tangent profiles of velocity and density (Hazel 1972), whence comes the expectation that the wavelength is about 7 times the shear layer thickness. In our computed modes, the mean value of λ/h_s is 7.4, the median value is 8.8, and 75% of the values of λ/h_s lie within the range [6, 11] (Fig. 13). Although it is likely that this ratio is altered by the range of naturally occurring shear profiles that spawn unstable modes (Part II), this result suggests that the Kelvin–Helmholtz model provides a reasonable description of the observed instabilities.

In sum, the apparent frequencies of predicted shear instabilities are close to f_{NB} (and close to $N/2\pi$ as well), the predicted vertical phase dependence of $\pi/2$ across h_s echoes the observed phase shifts, and 92% of the computed wavelengths are within a factor of 2 of $7h_s$.

7. Discussion

The LSA does not produce a preference for nighttime instabilities over daytime ones. Although this might be considered to be inconsistent with our interpretation of the narrowband signal (which has a strong daily variation, at least above 40 m, as indicated by Fig. 10) as shear instabilities, it may also be due to the relatively coarse quality of the data used to perform the LSA.

One of the great benefits of the TAO data is the long, freely available time series from which we can test theories such as ours. At the same time, we are pushing that data beyond its intended use as it is not resolved finely enough, either in time or in space, to adequately capture the true variability of shear and stratification in equatorial flows. This can be clearly seen by comparison to the richness of small-scale variability shown in the measurements of Moum et al. (2009). Perhaps of most concern is the lack of high-quality data near the surface where the downward migration of the mixed layer at night includes both the highly stratified and highly sheared mixed layer base, which is a potential instability trigger on a daily time scale. Yet, despite the limitations of the data, we have found that instabilities are predicted and that the properties of these instabilities are consistent with the properties of the observed narrowband oscillations. In a complementary future analysis, we will examine the well-resolved

measurements described by Moum et al. (2009) to determine if LSA can define the daily variations.

A detailed one-to-one comparison of observed and predicted instabilities is beyond the capability of the data available from the TAO moorings (which do not offer coincident velocity and density profiles). It may also be generally impossible simply because practically all instabilities (those characterized by $c \neq 0$) formed in sheared flows such as these are not observed until they have achieved observable amplitude. Hence, observed shear instabilities must coincide with mean flow conditions different from those in which they were created.

8. Summary and conclusions

These measurements provide a depiction of the narrowband oscillations at the equator that has not previously been available. They demonstrate the following characteristics:

- The oscillations are groupy. They appear as groups of $O(10)$ individual oscillations (Fig. 8).
- Spectral peaks at f_{NB} are approximately two orders of magnitude greater than at background frequencies, even when computed over two-day periods.
- f_{NB} is similar in magnitude to $N/2\pi$, but these are not correlated in time.
- Daily variation in oscillation potential energy is greatest at night and concentrated at the surface (Fig. 10).
- Mixing is enhanced (Fig. 11).
- There is high vertical coherence at f_{NB}.
- Finally, there exists strong vertical phase dependence at f_{NB}, typified by the abrupt $\pi/2$ phase shift in Fig. 7f.

At minimum, the observed abrupt vertical phase change motivates our interpretation of these oscillations as shear instabilities. Together with previous analyses (Sun et al. 1998; Smyth and Moum 2002) that have shown instability wavelengths comparable to observed wavelengths (Moum et al. 1992a), this has prompted the computation of the properties of shear instabilities from the available TAO data. From this analysis, we have shown that the localized shear layers where instabilities are formed are approximately $\lambda/7$ in thickness, with apparent frequencies comparable to f_{NB} (Fig. 9d), further supporting the case that the observed narrowband signal is due to shear instability resembling the classic Kelvin–Helmholtz form. This scenario differs from the model of a Doppler-shifted wave field suggested by McPhaden and Peters (1992).

These measurements support previous observations demonstrating the short-lived nature of packets of narrowband oscillations formed at night in the upper equatorial thermocline (McPhaden and Peters 1992; Moum et al. 1992a). The ratio $N_T^2\zeta^2/\epsilon_\chi$ may be considered a time scale representing the decay of the energy in the oscillations solely due to turbulence. This time scale is $O(1\text{ h})$ (Fig. 11), and it corresponds roughly to the observed duration of packets of $O(10$ periods) at 5 cph (in the reference frame of the fixed observer). The suggestion has been that the combination of space–time patchiness and high turbulence means these packets are generated locally and decay locally (Moum et al. 1992a). Our analysis indicates that the properties of these oscillations are consistent with shear instabilities formed from the hourly mean structure of currents and stratification.

It seems that the observed narrowband signal in the temperature record is consistent with locally generated shear instabilities that do not propagate or advect very far before breaking. The fact that f_{NB} is near $N/2\pi$ has to do with propagation of the spatial structure of the instability characterized by λ at c past the measurement point, rather than oscillation of a gravity wave at frequency N (Part II). In Part II, we show that N is a natural scale because 1) the dominant frequency of an ensemble of shear instabilities scales with S and 2) S and N are closely related in this near-critical Ri flow.

The strong variability in turbulence associated with that of these narrowband oscillations contributes to large variations in vertical mixing. It is important that we sample the full range of conditions to determine the complete role of mixing in the equatorial heat balance. The χpod measurements on TAO moorings are continuing with this objective.

Acknowledgments. This work was funded by the National Science Foundation (0424133, 0622922, and 0728375). Mike Neeley-Brown and Ray Kreth were responsible for construction of the χpods. Alexander Perlin helped to organize and process the data. Numerous NOAA personnel have aided this effort with their professional handling of our instruments on deployment and recovery. We are indebted to NOAA's TAO Project Office for continued support in χpod deployments and recoveries and for the use of the mooring data from 0°, 140°W.

REFERENCES

Baines, P. G., and H. Mitsudera, 1994: On the mechanism of shear flow instabilities. *J. Fluid Mech.,* **276,** 327–342.

Crawford, W. R., and T. R. Osborn, 1981: Control of equatorial currents by turbulent dissipation. *Science,* **212,** 539–540.

Fairall, C., E. Bradley, D. Rogers, J. Edson, and G. Young, 1996: Bulk parameterization of air-sea fluxes for Tropical Ocean–Global Atmosphere Coupled–Ocean Atmosphere Response Experiment. *J. Geophys. Res.,* **101** (C2), 3747–3767.

Gregg, M. C., H. Peters, J. C. Wesson, N. S. Oakey, and T. J. Shay, 1985: Intensive measurements of turbulence and shear in the Equatorial Undercurrent. *Nature,* **318,** 140–144.

Hazel, P., 1972: Numerical studies of the stability of inviscid parallel shear flows. *J. Fluid Mech.,* **51,** 39–62.

Howard, L., 1961: Note on a paper of John W. Miles. *J. Fluid Mech.,* **10,** 509–512.

Lien, R., M. J. McPhaden, and M. C. Gregg, 1996: High-frequency internal waves at 0°, 140°W and their possible relationship to deep-cycle turbulence. *J. Phys. Oceanogr.,* **26,** 581–600.

Mack, A. P., and D. Hebert, 1997: Internal gravity waves in the upper eastern equatorial Pacific: Observations and numerical solutions. *J. Geophys. Res.,* **102,** 21 081–21 100.

McCreary, J. P., 1981: A linear stratified ocean model of the Equatorial Undercurrent. *Philos. Trans. Roy. Soc. London,* **298A,** 603–635.

McPhaden, M. J., and H. Peters, 1992: Diurnal cycle of internal wave variability in the equatorial Pacific Ocean. *J. Phys. Oceanogr.,* **22,** 1317–1329.

Moum, J. N., and D. R. Caldwell, 1985: Local influences on shear flow turbulence in the equatorial ocean. *Science,* **230,** 215–315.

——, and J. D. Nash, 2009: Mixing measurements on an equatorial ocean mooring. *J. Atmos. Oceanic Technol.,* **26,** 317–336.

——, D. Hebert, C. A. Paulson, and D. R. Caldwell, 1992a: Turbulence and internal waves at the equator. Part I: Statistics from towed thermistors and a microstructure profiler. *J. Phys. Oceanogr.,* **22,** 1330–1345.

——, M. J. McPhaden, D. Hebert, H. Peters, C. A. Paulson, and D. R. Caldwell, 1992b: Internal waves, dynamic instabilities, and turbulence in the equatorial thermocline: An introduction to three papers in this issue. *J. Phys. Oceanogr.,* **22,** 1357–1359.

——, R.-C. Lien, A. Perlin, J. D. Nash, M. C. Gregg, and P. J. Wiles, 2009: Sea surface cooling at the equator by subsurface mixing in tropical instability waves. *Nat. Geosci.,* **2,** 761–765.

Pham, H. T., and S. Sarkar, 2010: Internal waves and turbulence in a stable stratified jet. *J. Fluid Mech.,* **648,** 297–324.

Skyllingstad, E. D., and D. W. Denbo, 1994: The role of internal gravity waves in the equatorial current system. *J. Phys. Oceanogr.,* **24,** 2093–2110.

Smyth, W. D., and W. Peltier, 1989: The transition between Kelvin-Helmholtz and Holmboe instability: An investigation of the overreflection hypothesis. *J. Atmos. Sci.,* **46,** 3698–3720.

——, and J. N. Moum, 2002: Waves and instability in an asymmetrically stratified jet. *Dyn. Atmos. Oceans,* **35,** 265–294.

——, ——, and J. D. Nash, 2011: Narrowband oscillations in the upper equatorial ocean. Part II: Properties of shear instabilities. *J. Phys. Oceanogr.,* **41,** 412–428.

Sun, C., W. D. Smyth, and J. N. Moum, 1998: Dynamic instability of stratified shear flow in the upper equatorial ocean. *J. Geophys. Res.,* **103** (C5), 10 323–10 337.

Turner, J. S., 1973: *Buoyancy Effects in Fluids*. Cambridge University Press, 367 pp.

Wijesekera, H., and T. M. Dillon, 1991: Internal waves and mixing in the upper equatorial ocean. *J. Geophys. Res.,* **96** (C4), 7115–7125.

Zaron, E. D., and J. N. Moum, 2009: A new look at Richardson number mixing schemes for equatorial ocean modeling. *J. Phys. Oceanogr.,* **39,** 2652–2664.